Scattering and Absorption Cross-sections of Atmospheric Gases in the Ultraviolet-Visible Wavelength Range (307 - 725 nm)

Quanfu He[1], Zheng Fang[1], Ofir Shoshamin[2], Steven S. Brown[3,4], Yinon Rudich[1,*]

[1] Department of Earth and Planetary Sciences, Weizmann Institute of Science, Rehovot 76100, Israel

[2] Department of Environmental Physics, Institute for Biological Research, Ness-Ziona 74100, Israel

[3] Chemical Sciences Division, Earth System Research Laboratory, National Oceanic and Atmospheric Administration, 325, Broadway, Boulder, CO 80305, USA

[4] Department of Chemistry, University of Colorado, 216 UCB, Boulder, CO 80309, USA

Correspondence to: Yinon Rudich (yinon.rudich@weizmann.ac.il)

Abstract

Accurate Rayleigh scattering and absorption cross-sections of atmospheric gases are essential for understanding the propagation of electromagnetic radiation in planetary atmospheres. Accurate extinction cross-sections are also essential for calibrating high finesse optical cavities and differential optical absorption spectroscopy and for accurate remote sensing. In this study, we measured the scattering and absorption cross-sections of carbon dioxide, nitrous oxide, sulfur hexafluoride, oxygen, and methane in the continuous wavelength range of 307–725 nm using Broadband Cavity Enhanced Spectroscopy (BBCES). The experimentally derived Rayleigh scattering cross-sections for CO_2, N_2O, SF_6, O_2, and CH_4 agree with refractive index-based calculations, with a difference of 1.5% and 1.1%, 1.5%, 2.9%, and 1.4% on average, respectively. The O_2-O_2 collision-induced absorption and absorption by methane are obtained with high precision at the 0.8 nm resolution of our BBCES instrument in the 307–725 nm wavelength range. New dispersion relations for N_2O, SF_6, and CH_4 were derived using data in the UV-vis wavelength range. This study provides improved refractive index dispersion relations, *n*-based Rayleigh scattering cross-sections, and absorption cross-sections for these gases.

Atmospheric
Chemistry
and Physics
Discussions

1. Introduction

28

29 The dominant interactions of gas-phase molecules with light in Earth's atmosphere can be divided

30 into absorption, where the light energy is converted to internal energy and generally (at

31 atmospheric pressures) transferred to the surrounding environment as either as heat or as

32 photoemission, and light scattering where the gases redistribute the light energy in the atmosphere.

33 The knowledge of light extinction (scattering + absorption) by gases is essential for predicting the

34 radiative transfer in the atmospheres of the Earth and other planets. In addition, the light extinction

35 by gases is widely used for determining the effective optical pathlength of high-finesse optical

36 cavities that measure trace gases and aerosols (Washenfelder et al., 2013; Washenfelder et al.,

37 2008; Wilmouth and Sayres, 2019; Jordan et al., 2019) and for Differential Optical Absorption

38 Spectroscopy (DOAS) to infer information about the light extinction properties of aerosols and

39 clouds in the open atmosphere (Baidar et al., 2013; Platt and Stutz, 2008).

40 The interaction of light with a wavelength much larger than the size of a molecule/particle gives

41 rise to the scattering of light, which is known as Rayleigh scattering(Strutt, 1899). Rayleigh

42 scattering accounts for scattering, local field effects (Lorentz–Lorenz) (Strutt, 1920) as well as

43 depolarization from the non-sphericity of molecule/particles (King correction factor) (King and

44 Eve, 1923; Strutt, 1918). For gas with known refractive index (n_v) and King correction factor

45 ($F_k(v)$), the wavelength-dependent Rayleigh scattering cross-section (σ_v, cm^2 molecule^{-1}) can be

46 calculated as follows (Sneep and Ubachs, 2005):

47 $$\sigma_v = \frac{24\pi^3 v^4}{N^2}\left(\frac{n_v^2-1}{n_v^2+2}\right)^2 F_k(v) \tag{1}$$

48 where N is the number density of the gas (molecules cm^{-3}) and v is the wavenumber of the light

49 (cm^{-1}). Note that the cross-section contains the gas number density but is not in fact dependent on

50 the number density since the refractive index also appears in the expression. This n-based method

51 is an advantageous approach for calculating Rayleigh scattering cross-sections, but it is vital to

52 note that the accuracy of the calculated cross-sections depends on the experimentally-determined

53 refractive index and the King correction factors. In particular, cautions should be used when

54 applying a dispersion formula derived from measurements in one wavelength region to calculate

55 Rayleigh scattering cross-sections in a different wavelength range.

Atmospheric
Chemistry
and Physics
Discussions

Open Access
EGU

56 Direct experimental measurement of Rayleigh scattering cross-sections is essential given the

57 potential uncertainties in n-based calculations. While measurements of the King correction factors

58 and refractive index for gases are well known from the literature (Cuthbertson and Cuthbertson,

59 1932; Leonard, 1974; Strutt, 1920; Vukovic et al., 1996; Hohm, 1993), there are only a few direct

60 measurements of Rayleigh scattering cross-sections (Ityaksov et al., 2008a, b; Jordan et al., 2019;

61 Naus and Ubachs, 2000; Sneep and Ubachs, 2005; Thalman and Volkamer, 2013; Thalman et al.,

62 2014; Wilmouth and Sayres, 2019; He et al., 2018; Fuchs et al., 2009), especially measurements

63 with a continuous spectrum from ultraviolet to visible.

64 Rayleigh scattering cross-section measurements were previously performed at a single wavelength

65 (e.g., 458 nm, 532 nm, 632.8 nm) using Nephelometry (Shardanand and Rao, 1977) and cavity-

66 ring down spectroscopy (CRDS) (Ityaksov et al., 2008a, b; Naus and Ubachs, 2000; Sneep and

67 Ubachs, 2005; He et al., 2018). More recently, advanced Broadband Cavity Enhanced

68 Spectroscopy (BBCES) was used to determine the Rayleigh scattering cross-sections of gases such

69 as Ar, CO_2, O_2, SF_6, and CH_4. The BBCES technique enables the measurement of Rayleigh

70 scattering cross-sections over a broad wavelength range. Thalman et al. (2014) performed

71 measurements over selected wavelength regions between 350 and 660 nm using six BBCES

72 cavities for N_2, Ar, and O_2. The BBCES were calibrated with He and N_2 using Rayleigh scattering

73 cross-sections calculated using their refractive index and from cavity-ring down measurements,

74 respectively. They found a good agreement with n-based values to within 0.2±0.4%. Recent studies

75 using BBCES with 30 nm spectral range were also used for Rayleigh scattering cross-section

76 measurement in the UV wavelength region and demonstrated excellent agreement with n-based

77 values for Ar and CO_2 (Wilmouth and Sayres, 2020, 2019). Recently, Rayleigh scattering cross-

78 sections for CO_2 were measured using BBCES at visible wavelengths between 400 and 650 nm,

79 and agreement with n-based values was within 2.4% on average. To the best of our knowledge,

80 there is no direct continuous wavelength measurements of extinction cross-sections of gases that

81 covers the ultraviolet across the entire visible range (300–725 nm) as shown in Table 1.

82 In this study, we used a recently-developed BBCES instrument to measure the extinction cross-

83 sections of CO_2, N_2O, SF_6, O_2, and CH_4 continuously across the wavelength region 307–725 nm.

84 All of the measurements were done at a single pressure to eliminate effects due to alignment. This

85 requires the use of two gases with different Rayleigh cross-sections for the calibration of the

86 BBCES instrument since the reference state is not vacuum. In this study, He and N_2 were used to

87 calibrate the system. By using the *n*-based calculated Rayleigh scattering cross-sections of He and

88 N_2 to calibrate the path length of the optical cavity, the other cross-sections can be determined

89 relative to the difference between these two gases. We report high accuracy Rayleigh scattering

90 cross-sections for all five gases and compared our results with previous *n*-based values. New

91 dispersion relations for N_2O, SF_6, and CH_4 are derived by incorporating data obtained by this study,

92 extinction cross-section data in the deep UV, and previously available scattering cross-section data

93 in the visible wavelength range.

94

95 **2. Methods**

96 **2.1 Extinction measurement using BBCES**

97 The BBCES systems used in this study are analogous to our previous studies (He et al., 2018;

98 Washenfelder et al., 2016; Bluvshtein et al., 2016). Briefly, our BBCES consists of two channels,

99 one in the UV (BBCES$_{UV}$, 307-350 nm) and one in the UV-vis range (BBCES$_{Vis}$, 338-725 nm).

100 The two channels of the BBCES share a laser-driven Xenon arc lamp source (LDLS EQ−99CAL,

101 Energetiq Technology, Inc., MA, USA) coupled with a high transmission UV-Vis optical fiber

102 from which the light is collimated and focused (BBFIBERX-600-1M, Energetiq Technology, Inc.,

103 MA, USA). The light source was purged with high purity N_2 and cooled by an aluminum block

104 (with 15℃ circulating water inside) to maintain stable optical power output. The UV light from

105 the fiber is reflected by a low-pass dichroic mirror and filtered into the BBCES$_{UV}$ channel, which

106 has a cavity with two 2.5 cm diameter, 1 m radius of curvature mirrors, with manufacturer's

107 reported reflectivity of 0.9995 (per pass loss = 500 parts per million, ppm) at the nominal center

108 wavelength of 330 nm (Advanced Thin Films, Boulder, USA). The transmitted UV-vis light from

109 the beam splitter is reflected and filtered into the BBCES$_{Vis}$ channel consisting of two 2.5 cm, 1 m

110 radius of curvature mirrors (FiveNine Optics, USA) with manufacturer's reported reflectivity

111 above 0.9993 (loss < 700 ppm), see Figure S1. The light emerging through the rear mirror of the

112 cavity was focused using a 0.1 cm F/2 fiber collimator (74−UV, Ocean Optics, Dunedin, FL, USA)

113 into a high transmission UV-vis optical fiber which directs the light into a high-performance

114 spectrometer (QEPro, Ocean Insight, USA). Before gas measurement, the wavelength of the

115 spectrometer was calibrated using an HG-1 mercury argon calibration light source (Ocean Insight,

116 USA) within the wavelength range of 302.15−727.29 nm. During these experiments, a 300 line

117   mm^{-1} grating and a 200 μm entrance slit width were used. The CCD array is a back-illuminated

118   detector with 1024×56 pixels (Hamamatsu S7031-1006, Japan) thermo-electrically cooled to −10 ℃

119   to reduce thermal noise. Individual spectra at a wavelength resolution of 0.8 nm were acquired

120   with 3.0 s integration time, and a total of 150 spectra were recorded during each measurement.

121   During the extinction measurements, the entire 94.0 ± 0.1 cm pathlength between the mirrors was

122   filled with He, N_2, CO_2, N_2O, SF_6, or CH_4. The gases were obtained from several vendors (Airgas,

123   Linde) with the following purities: He, 99.995%; N_2, 99.999%; N_2O, 99.999%, CO_2, 99.999%;

124   SF_6, 99.999%; CH_4, 99.9995%.

125   The reflectivity of the mirrors (R(λ)) can be determined as a function of wavelength (λ) by taking

126   into account the difference in the extinction due to known literary data of Rayleigh scattering

127   coefficient (α_{Ray}^{gas}) by two different gases such as N_2 ($\alpha_{Ray}^{N_2}(\lambda)$) and He ($\alpha_{Ray}^{He}(\lambda)$) (Washenfelder

128   et al., 2008).

129
$$\frac{1-R(\lambda)}{d} = \frac{I_{N_2}(\lambda)\left(\alpha_{Ray}^{N_2}(\lambda)\right) - I_{He}(\lambda)\left(\alpha_{Ray}^{He}(\lambda)\right)}{I_{He}(\lambda) - I_{N_2}(\lambda)}$$
(2)

130   where d is the length of the cavity filled by the gas. In this study, the studied gas filled the entire

131   length of the cavity (94.0 ± 0.1 cm) since no purge flows were used. I_{gas} is the light intensity

132   measured by filling the cavity with high purity N_2 ($I_{N_2}(\lambda)$) and He ($I_{He}(\lambda)$). Rayleigh scattering

133   (α_{Ray}^{gas}) is the combined product of Rayleigh scattering cross-section (σ) and the gas number density

134   (N) during the measurements. Rayleigh scattering cross-sections of N_2 and He are calculated using

135   the data in Table 1. Figure S1 shows typical examples of light intensity when the BBCES cavities

136   are filled with pure N_2. Reflectivity measurements were repeated every three sample measurements

137   to track the stability of the system.

138   Once the reflectivity is determined, it is possible to calculate the wavelength-dependent extinction

139   cross-sections of other gases ($\sigma(\lambda)$) as follows:

140    $$\sigma(\lambda) = \left[\left(\frac{1-R(\lambda)}{d}\right)\left(\frac{I_{He}(\lambda) - I_{gas}(\lambda)}{I_{gas}(\lambda)}\right) + \left(\frac{I_{He}(\lambda)}{I_{gas}(\lambda)}\right)\left(\alpha_{Ray}^{He}(\lambda)\right)\right]/N$$
(3)

141   Where N is the number density of the gas during the measurements, and $I_{gas}(\lambda)$ is the light intensity

142   when a target gas fills the cavity. During our experiments, the purge flow of the high reflection

143 mirrors was shut down to ensure that the cavity was filled with target gas completely. To measure

144 the extinction cross-sections of CO_2, N_2O, and SF_6, the cavity is filled with pure target gas. Mass

145 flow controller controlled O_2/CH_4 flow was mixed with He in a 2 m Teflon tube ($\Phi = ¼$ inch) to

146 generate a gas mixture with total flow rate of 500 mL min^{-1}. For O_2 experiments, measurements

147 were performed for O_2 + He mixtures by varying the O_2 percentage between 10% and 100% with

148 a 10% step. The CH_4, measurements were performed for CH_4 + He mixtures with CH_4 percentage

149 ranges between 10% to 100% with a 10% step. Additional measurements were also performed for

150 15%, 25%, 35%, and 45% CH_4.

2.2 Extinction measurements using cavity-ring down systems (CRDS) at 404 nm and 662 nm.

152 To obtain independent measurements for the extinction cross-sections and to cross-validation of

153 the BBCES technique, we conducted CRD measurements at two fixed wavelengths of 404 nm and

154 662 nm. CRDS is a highly sensitive technique and uses a different measurement principle than

155 BBCES. The CRDS measured the decay rate of light due to extinction rather than an absolute

156 absorbance (as in the BBCES) and thus immune to shot-to-shot source light fluctuations. A

157 detailed description of the CRD method for light extinction measurement can be found in

158 Bluvshtein et al. (2016) and He et al. (2018). Briefly, diode lasers (110 mW 404 nm diode laser,

159 iPulse, Toptica Photonics, Munich, Germany; 120 mW 662 nm diode laser, HL6545MG, Thorlabs

160 Inc., NJ, USA) are used as the light source of these CRDS. The 404 nm and 662 nm lasers are

161 modulated at 1383 Hz and 500 Hz with a 50% duty cycle. The diode lasers are optically isolated

162 by quarter waveplates (1/4 λ) and polarizing beam splitters to prevent damage to the laser head by

163 back reflections from the highly reflective CRDS mirror. The back-reflected light beam is directed

164 into a photodiode, which serves as an external trigger source. Light transmitted through the back

165 mirror of the cavity is collected by an optical fiber and detected by a photomultiplier tube (PMT),

166 which samples at a rate of 10 to 100 MHz. The time-dependent intensity data is acquired with a

167 100MHz card (PCI-5122, National Instruments, USA) and processed by data acquisition software

168 in Labview. An exponential curve is fitted to each intensity decay data set (Figure S2). Over 1000

169 decay time measurements are monitored and averaged on a second basis. The residual of the fit

170 for the averaged intensity decay is obtained and further normalized to the averaged intensity. The

171 derived relative residuals (Figure S2) show no apparent structure with other time constants,

172 validating the application of CRDS as a good measure of extinction. The resultant 1 Hz decay time

173 is averaged over one measurement duration of five minutes with standard error as the measurement

174 uncertainty.

175 All of the CRDS measurements were performed under room temperature and pressure downstream

176 from the BBCES instrument. The gas temperature (K-type thermocouple) and cavity pressure

177 (Precision Pressure Transducer, Honeywell International Inc., MN, USA) were recorded for gas

178 number density (N) calculation. During the CRDS measurements, the full cavity was filled with

179 the investigated gases (He, CO_2, N_2O, SF_6, O_2, CH_4, or gas mixtures (O_2 + He and CH_4 + He)).

180 The extinction cross-section ($\sigma(\lambda)$) of the studied gas was measured relative to that of He and was

181 calculated by equation (4):

182 $$\sigma(\lambda) = \frac{L}{clN}\left(\frac{1}{\tau_{gas}} - \frac{1}{\tau_{He}}\right) + \sigma_{He} \tag{4}$$

183 Where L is the total length of the cavity (l), c is the speed of light, and $\tau_{gas \text{ and }} \tau_{He}$ are the ring-down

184 time of the cavity when it is filled by target gas or by the reference gas, He.

185 **2.3 Data processing**

186 For comparison, the scattering cross-sections of the gases investigated in this study were also

187 calculated with Equation (1) based on the refractive index and the King correction factors available

188 in the literature that are listed in Table 1. The King correction factors are taken as unity for mono-

189 atomic molecules and spherical molecules (with regards to the depolarization) but deviates for

190 non-spherical molecules. For the 307–725 nm wavelength range of this study, the n-based

191 calculated Rayleigh scattering cross-sections from largest to smallest are SF_6, N_2O, CO_2, CH_4, N_2,

192 O_2, and He.

193 The extinction of O_2 + He mixtures (α_{O_2+He}) consists of the extinction by O_2 (α_{O_2}) and He (α_{He}),

194 and the O_2–O_2 collision-induced absorption ($\alpha_{O_2-O_2}$). The extinction of O_2 and He is a combined

195 product of extinction cross-section (σ_{gas}) and gas number density (N_{gas}). Thus α_{O_2+He} can be

196 described with the following equation:

197 $$\alpha_{O_2+He} = \sigma_{O_2-O_2} \times N_{O_2}^2 + \sigma_{O_2} \times N_{O_2} + \sigma_{He} \times N_{He} \tag{5}$$

198 Where N_{O_2} and N_{He} are the number density of the O_2 and He in the cavities. Performing a 2rd order

199 polynomial fit to the extinction obtained by the BBCES with respect to the gas number density

200   thus yields the extinction cross-section of O_2 and the O_2-O_2 collision-induced absorption (CIA)

201   cross-section.

202   In addition to the results from 2rd order polynomial fitting, we also used data from pure O_2

203   measurement to calculate the extinction by O_2 and by CIA of O_2–O_2. The real refractive index of

204   O_2 (n_{O_2}) derived from extinction data measured in the wavelength regions where there is no

205   absorption was fitted using the generalized expression of $(n_{O_2} - 1) \times 10^8 = A + \frac{B}{C - v^2}$. Based on

206   the refractive index, the scattering cross-sections of O_2 in the wavelength range of 307-725 nm

207   were further calculated. By subtracting the scattering cross-section of O_2 from the measured total

208   extinction, we derived the CIA of O_2–O_2. However, the O_2 absorption bands at 580, 630, and 690

209   nm overlaps with those of O_2–O_2 collisions. Additional corrections are thus needed to split the

210   absorption by O_2 and O_2–O_2 collision, which is out of the scope of this study.

211   Methane has weak vibrational overtone absorption in the UV-vis wavelength range that is

212   comparable to or greater than its Rayleigh scattering. Previous high-resolution spectroscopy

213   studies have identified smooth and unstructured absorption bands across the UV-visible range

214   (Giver, 1978; Smith et al., 1990). The spectral features are substantially broader than 0.8 nm, thus

215   the absorption by CH_4 can be measured by our BBCES. The measured extinction coefficients of

216   CH_4+He mixtures (α_{CH_4+He}) are linearly correlated with the number concentration of the CH_4 (N_{CH_4})

217   as described by the following equation:

218    $\alpha_{CH_4+He} = \sigma_{CH_4} \times N_{CH_4} + \sigma_{He} \times N_{He}$ (6)

219   A linear fit was used for deriving the extinction cross-section of CH_4. The absorption between 300

220   and 400 nm is negligible as compared to the Rayleigh scattering. Thus extinction data in this UV

221   wavelength range were used to calculate the real part of the refractive index of CH_4 which was

222   further fitted utilizing the expression of $(n_{CH_4} - 1) \times 10^8 = A + \frac{B}{C - v^2}$. By applying this

223   dispersion relation, the Rayleigh scattering cross-sections in the entire wavelength range of 307–

224   725 nm were derived. Finally, the CH_4 absorption cross-sections were calculated by subtraction of

225   the scattering cross-section from the extinction cross-section.

226   **2.4 Error Propagation for BBCES**

227 The uncertainty for BBCES measurements can be assessed by the propagation of the errors

228 associated with the measurements. The pressure ($\pm$0.01%), temperature ($\pm$0.1%) and cavity length

229 (94.0 $\pm$ 0.1 cm) are combined with the Rayleigh cross-section uncertainties for N_2 ($\pm$1%) as well

230 as uncertainty in the measurements of the spectral signal by the spectrometer ($\ll$0.2%) to get an

231 overall relative uncertainty for the mirror reflectivity curve of $\pm$1.03%. This uncertainty is further

232 propagated to the target gas by consideration of the uncertainties of pressure, temperature, and

233 spectral intensity of the target gas measurements. The overall 1-σ uncertainty of the gas extinction

234 cross-section is 1.1%. The precision of the mass flow controllers is 0.5 mL min^{-1}. When the total

235 flow rate is 500 mL min^{-1}, the resulted uncertainty of the gas concentration (10-100%) varies from

236 0% to 1.0%. Thus, the overall 1-σ uncertainty of extinction coefficients measured for CH_4+He and

237 O_2+He varies from 1.1% to 1.5%. The detailed wavelength-dependent uncertainties were

238 calculated due to the wavelength-dependence of the spectral intensity. The results are shown and

239 discussed in later sections.

240

241 **3 Results and Discussion**

242 **3. 1 Performance of the optical system**

243 The reflectivity of the cavity mirrors, measured across the entire range using the difference in

244 Rayleigh scattering of N_2 and He, was very stable throughout the experiments. The measured

245 mirrors reflectivity curves are shown in Figure S1. The mean peak reflectivity of the BBCES$_{UV}$

246 mirrors was 0.999328$\pm$0.000006 (672$\pm$6 ppm) at 330 nm, with a corresponding effective optical

247 pathlength of 1.40$\pm$0.01 km. The reflectivity curve of the BBCES$_{Vis}$ is much more structured, with

248 reflectivity ranging between 0.999224$\pm$0.000010 and 0.9999550$\pm$0.0000006 (776$\pm$10 ppm > loss >

249 45$\pm$0.6 ppm) over a wide wavelength range of 338–725 nm. The reflectivity of the BBCES$_{Vis}$ is

250 much higher than that of our previous system (He et al., 2018) and also covers a much broader

251 wavelength range. Thus the effective pathlength of the BBCESVis varies between 1.3 and 20.4

252 km, guaranteeing a high sensitivity of the extinction measurement. The mean uncertainty in the

253 effective pathlength across the measured wavelengths as determined from the mirror reflectivity

254 was $\pm$1.03%, which is predominantly due to the uncertainty in the Rayleigh scattering cross section

255 for N_2 derived from *n*-based calculation.

256 **3. 2 Rayleigh scattering cross-sections of CO_2, N_2O, SF_6.**

257 Figure 1 shows the extinction cross-sections of CO_2, N_2O, and SF_6 measured by the BBCES. The

258 extinction cross-sections of these gases monotonically decrease with increasing wavelength, and

259 no absorption (i.e., no structured extinction larger than the smoothly varying Rayleigh curve) is

260 observed in the wavelength range of 307–725 nm, indicating that the measured extinction is due

261 solely to the Rayleigh scattering of these gases. The wavelength-dependent relative standard

262 deviations of the measurements for each gas are shown in Figure 1d. The mean 1-σ uncertainty of

263 the reported cross sections for all three gases across the 307–725 nm wavelength range is 1.5% for

264 CO_2, 1.1% for N_2O, and 1.5% for SF_6. As mentioned above, the derived uncertainty originates

265 predominantly from the uncertainty in the N_2 Rayleigh scattering cross-section. Uncertainty in the

266 Rayleigh cross-sections of each gas varies with wavelength and generally tracks the light intensity

267 spectra, which is a combined product of light source spectrum and the mirror reflectivity profile.

268 The uncertainty is much higher when the transmitted light intensity is low (Figure S1).

269 The BBCES measured Rayleigh scattering cross-sections for these three gases agree well with

270 those obtained by our CRDS operating at 404 nm and 662 nm, with deviations smaller than 1.6%.

271 Table 2 listed the Rayleigh scattering cross-sections at several wavelengths obtained by the

272 BBCES measurements (Exp) and by the theoretical calculations using the refractive index and $F_k(v)$

273 values from Table 1 (*n*-based). The relative differences between these two sets of results are within

274 1.4%.

275 Figure 1a–c shows a comparison of the measured Rayleigh scattering cross-sections for CO_2, N_2O,

276 and SF_6 with *n*-based calculations and with previous experimental results from the literature. There

277 are a few measurements for the Rayleigh scattering cross-sections for CO_2 which cover a wide

278 spectral range (Jordan et al., 2019; Shardanand and Rao, 1977; Sneep and Ubachs, 2005; Wilmouth

279 and Sayres, 2019; He et al., 2018). There are fewer Rayleigh scattering measurements for N_2O and

280 SF_6 in the studied wavelength range. The measured Rayleigh scattering cross-sections for CO_2,

281 N_2O, and SF_6 are in excellent agreement with *n*-based calculation. The wavelength-dependent

282 difference of our experimentally derived Rayleigh scattering cross-sections with *n*-based

283 calculations are shown in Figure 1e. The mean ratios of our measurements to the n-based values

284 for the entire wavelength range of 307–725 nm are 1.00 ±0.01, 0.99±0.01, and 1.01±0.01 for CO_2,

285 N_2O, and SF_6, respectively. Notably, while our results for N_2O agree well with the *n*-based

286 calculations, previous results obtained by CRDS at 532 nm (Sneep and Ubachs, 2005) and by

287 absorption spectroscopy in the wavelength of 300–315 nm (Bates and Hays, 1967) do not agree

288 well with the n-based calculations. The measurements between 300 and 315 nm were first

289 published by Bates and Hays (1967), who obtained the results from a doctoral thesis. However,

290 the results from our BBCES system are in good agreement with the *n*-based calculations and with

291 experimental results from independent CRDS measurements, thus increasing the confidence in our

292 measured values.

3. 3 Scattering and absorption cross-sections of O_2.

294 The UV-vis spectra of gas-phase molecular oxygen are characterized by discrete structured

295 absorption bands due to the electronic transition $(b^1\sum_g^+(v'=1/2/3) \leftarrow \sum_g^-(v''=0))$ of O_2

296 monomer, broader unstructured CIA of O_2–O_2, and structured dimer bands from the bound van

297 der Waals O_2 dimer (Newnham and Ballard, 1998). Under atmospheric conditions, the O_2–O_2 CIA

298 bands are frequently described as "O_4" bands, although absorption by O_2 dimer is thought to be

299 significant only under very low-temperature conditions (Thalman and Volkamer, 2013; Long and

300 Ewing, 1973). Within the wavelength range investigated in this work, the molecular oxygen B

301 band at 688 nm $(b^1\sum_g^+(v'=1) \leftarrow X^3\sum_g^-(v''=0))$, γ overtone band at 629 nm $(b^1\sum_g^+(v'=2) \leftarrow$

302 $X^3\sum_g^-(v''=0))$, and δ overtone band at 580 nm $(b^1\sum_g^+(v'=3) \leftarrow X^3\sum_g^-(v''=0)$ overlap with

303 O_2–O_2 CIA bands of $^1\sum_g^+(v=1)$, $^1\Delta_g + ^1\Delta_g (v=0)$, and $^1\Delta_g + ^1\Delta_g (v=1)$, respectively.

304 These absorption bands can only be resolved by a high-resolution spectroscopic technique.

305 Absorption cross-sections of the B, γ, and δ bands were convoluted from the HITRAN database

306 (Gordon et al., 2017) by considering the temperature, pressure, and instrument's wavelength

307 resolution. The wings of the oxygen lines also show a quadratic dependence on the pressure due

308 to pressure broadening. However, due to the minimal O_2 absorption contribution below 680 nm

309 and the low instrument wavelength resolution, the extinction cross-section of the O_2 monomer can

310 be treated as linearly correlated with the O_2 concentration. Moreover, the O_2–O_2 CIA cross-section

311 is correlated with the square of the O_2 concentration. Therefore, these cross-sections can be

312 retrieved from measurements at different O_2 concentrations. Due to the discrete structured

313 absorption bands and the instrument's wavelength resolution, the range of absorption cross-

314 sections spans several orders of magnitude within the spectral response of the instrument, limiting

315 the relevance of the absorption cross-sections for other researchers. These results are not further

316 discussed here. However, the data for broader unstructured CIA of O_2–O_2 are still useful for

317 various applications.

Atmospheric
Chemistry
and Physics
Discussions

Open Access
EGU

318   Figure 2 shows the wavelength-dependent extinction coefficients of O_2+He mixtures. He was used

319   in these experiments to minimize extinction contributions from Rayleigh scattering. Nine

320   absorption peaks centered at 344 nm (CIA), 360 nm (CIA), 380 nm (CIA), 446 nm (CIA), 477 nm

321   (CIA), 532 nm (CIA), 577 nm (δ overtone and CIA), 629 nm (γ overtone and CIA), and 688 nm

322   (B band and CIA) were observed in the wavelength range of 307–725 nm. The absorption

323   coefficients of the central wavelengths for the first eight peaks increase non-linearly with O_2

324   concentration while that of the 688 nm peak increases in a more linear manner, indicating that the

325   O_2 B band absorption dominates the last absorption peak while the other peaks are mostly

326   associated with CIA of O_2-O_2.

327   The extinction coefficients obtained by the BBCES correlated well with those measured by the

328   CRD, with slops of 0.990 (R^2=0.9994) and 0.993 ($R^2 = 0.9996$) at the wavelengths of 404 nm and

329   662 nm, respectively (Figure 3). This excellent agreement between the instruments further

330   substantiates the BBCES measurements and suggests that the accuracy of the BBCES is better

331   than estimated in the error propagation above, where the N_2 refractive index was the largest

332   uncertainty. As explained in the data processing section, the measured extinction coefficients were

333   fitted with a 2rd order polynomial (selected wavelengths at the peaks of the CIA absorption bands

334   are shown in Figure 4). At 476.7, 577.2, and 629.2 nm, the absorption is from the CIA of O_2–O_2.

335   The fit generates positive values matching the absorption cross-section of O_2–O_2 CIA. At 687.7

336   nm where strong B-band absorption appears, the fit yields a small negative coefficient for O_2–O_2

337   CIA.

338   Figure 5a shows the extinction cross-section measured for 100% O_2. These results agree well with

339   previously reported results by Jordan et al. (2019). For wavelengths where no absorption is

340   detected, the measured extinction cross-sections agree well with n-based calculations. Figure 5b-

341   c shows the determined extinction cross-sections for molecular O_2 and the absorption cross-

342   sections of O_2–O_2 CIA. For wavelength ranges without O_2 bands, our extinction cross-sections

343   agree well with n-based values with an average deviation of 2.8%. The absorption cross-sections

344   for O_2–O_2 CIA derived in this study mostly agree well with literature data from Thalman and

345   Volkamer (2013). The differences are within 1.1% at 477, 532, 577, and 630 nm but larger

346   deviations were found at 344 (4.2%), 360 (-29%), 380 (-21%), and 446 (4.2%) nm. These

347   absorption bands are the lowest intensity bands and therefore have the largest relative uncertainties

348   in either measurement.

349   The Rayleigh scattering cross-sections of molecular O_2 derived from the 100% O_2 measurement

350   agree well with n-based calculations with an average difference of 1.2%. CIA of O_2–O_2 calculated

351   from this single measurement matches the results from the fitting method. Due to strong absorption

352   from O_2 B band and γ overtone band, this method cannot derive the cross-sections of CIA of O_2-

353   O_2 at 630 and 688nm.

3. 4 The scattering and absorption cross-sections of CH_4.

355   CH_4 has weak absorption in the UV–vis wavelength range, and these bands dominate the

356   photographic spectra of planets such as Uranus and Neptune. Figure 6 presents the wavelength-

357   dependent extinction coefficients of CH_4+He mixtures. A total of eleven absorption bands were

358   detected in the wavelength range of 307–725 nm. The extinction coefficients increase as a function

359   of increasing CH_4 concentration. Extinction coefficients obtained by the BBCES correlated well

360   with those measured in parallel by the CRDS, with slopes of 1.002 (R^2=0.9999) and 0.99 ($R^2 =$

361   0.999) at the wavelengths of 404 nm and 662 nm (Figure S3). The excellent agreement between

362   these three systems further supports the accuracy of BBCES extinction measurements over a wide

363   working range. The measured extinction coefficients were linearly fit against the CH_4 number

364   concentration. Figure 7 shows the fitted curves at five selected wavelengths. The extinction

365   coefficients have a linear correlation with CH_4 concentration ($R^2 > 0.9988$) without exception. The

366   calculated slopes represent the extinction cross-sections of CH_4 and also indicate a wide dynamic

367   range of our BBCES.

368   The extinction cross-sections for CH_4 retrieved from concentration-dependent measurements are

369   plotted in Figure 8a. BBCES results from this study agree well with results from previous studies

370   using BBCES (Jordan et al., 2019; Wilmouth and Sayres, 2019) and CRDS (Sneep and Ubachs,

371   2005). Previous studies using a Nephelometer (Shardanand and Rao, 1977) and interferometer

372   (Cuthbertson and Cuthbertson, 1920; Watson et al., 1936) obtained the scattering cross-sections

373   of CH_4. The BBCES measures the extinction cross-section. For wavelengths where extinction is

374   dominated by Rayleigh scattering (< 475 nm), our BBCES results agree well with the results from

375   Nephelometer and interferometer measurements. In this study, the refractive index of CH_4 was

376   calculated using the extinction data in the wavelength range of 307-400 nm. The calculated

377   refractive index was fitted to the general expression:

378    $(n_{CH_4} - 1) \times 10^8 = 5476 + \frac{4.1579 \times 10^{14}}{1.1568 \times 10^{10} - \nu^2}$ (7)

379   As shown in Figure 8b, our calculated scattering cross-sections are in good agreement with those

380   derived from the newest refractive index developed by Wilmouth and Sayres (2020) (Table 2),

381   with an average difference of 1.4%. The absorption cross-section, which is the difference between

382   the total extinction and the Rayleigh scattering cross-section, is shown in Figure 8c. At most

383   spectral ranges, our results are in good agreement with the results from previous studies (Giver,

384   1978; Smith et al., 1990). For example, the difference as compared to the results from Giver (1978)

385   at 542, 576.4, 598, 619, 665.7, and 703.6 nm is 4.0% on average. At several wavelength regions

386   (e.g., 520–536nm, 580–605 nm), the results from Fink et al. (1977) differ from all of the other

387   studies. In the wavelength range of 400–725 nm, absorption contributes up to 99.7% of the CH_4

388   extinction.

389   **3. 5 Dispersion relations for N_2O, SF_6 and CH_4.**

390   **SF_6:** Wilmouth and Sayres (2020) found that their measured Rayleigh scattering cross-sections for

391   SF_6 in the ultraviolet range were much lower than those from the n-based expression of Sneep and

392   Ubachs (2005). To better constrain the dispersion formula when extrapolated over a broad

393   wavelength range, we employed an alternative fit of the form $A+B/(C–v^2)$ to our data. The

394   Rayleigh scattering derived refractive index in the wavelength range of 264-297 nm and 333-363

395   nm by Wilmouth and Sayres (2020, 2019), and direct refractive index measurement at 632.99 nm

396   (Vukovic et al., 1996) were used (Figure 9a). The resulting dispersion relation for SF_6 in the

397   wavelength range of 264–725 nm is

398   $$(n_{SF_6} - 1) \times 10^8 = 22871 + \frac{8.0021 \times 10^{14}}{1.6196 \times 10^{10} - v^2}$$ (8)

399   **N_2O:** Sneep and Ubachs (2005) derived the refractive index based on polarizability measurements

400   using interferometer at five single wavelengths (457.9, 488, 514.5, 568.2, 647.1 nm) by Alms et

401   al. (1975). In this study, we calculated the refractive index of N_2O from the Rayleigh scattering

402   cross-sections in the wavelength range of 307–725. Based on this refractive index data set, the

403   dispersion relation (Eq (9)) for N_2O was retrieved for a much broader wavelength range (Figure

404   9b) compared to that generated by Sneep and Ubachs (2005).

405   $$(n_{N_2O} - 1) \times 10^8 = 23154 + \frac{1.534 \times 10^{14}}{6.5069 \times 10^9 - v^2}$$ (9)

406   **CH_4:** The previous study by Wilmouth and Sayres (2019) has shown that their measured Rayleigh

407   scattering cross-sections for CH_4 are in substantial disagreement (22%) with those calculated from

408   the refractive index recommended by Sneep and Ubachs (2005). Sneep and Ubachs (2005)

409   formulated the refractive index of CH_4 based on interferometric measurements at wavelengths of

410   325, 543.5, 594.1, 612, and 633 nm by Hohm (Hohm, 1993). However, the Rayleigh scattering

411   cross-sections calculated from their refractive index are much higher than all the measured values

412   listed in Figure 9b. Using Rayleigh scattering cross-sections in the wavelength range of 264–297

413   nm, 333–363 nm (Wilmouth and Sayres, 2019, 2020), 307–400 nm from this study, and single

414   wavelength measurements which are not impacted by absorption (Cuthbertson and Cuthbertson,

415   1920; Shardanand and Rao, 1977; Watson et al., 1936), we derived the dispersion formula for the

416   refractive index of CH_4 in the combined UV/visible range (Figure 9c) as follows:

417    $(n_{CH_4} - 1) \times 10^8 = 7327.7 + \frac{4.1884 \times 10^{14}}{1.2208 \times 10^{10} - \nu^2}$ (10)

418   The calculated Rayleigh scattering cross-sections using the dispersion relations derived in this

419   study were compared with those derived from previously recommended formulations listed in

420   Table 1 (Figure 9). The difference increases significantly at the longer wavelength in the region of

421   320–725 nm (Figure S4). The average deviations are 0.8%, 0.9%, and 1.6% for SF_6, N_2O, and CH_4,

422   respectively. Notably, the difference for CH_4 is much more significant than for the other two gases.

423   This study uses additional measurements and literature data in the wavelength ranges of 307-

424   333nm and 363–400 nm than those used by Wilmouth and Sayres (2020). Therefore this fit

425   captures well our BBCES measurements (Figure 9d), and also the Wilmouth and Sayres (2020,

426   2019) data.

Conclusions and Implications

428   Rayleigh scattering cross-sections between 307 and 725 nm were determined for CO_2, N_2O,

429   SF_6, O_2, and CH_4 by simultaneous BBCES and CRDS measurements. Extinction coefficients

430   obtained by the BBCES show high consistency with those measured by parallel CRDS at 404 and

431   662 nm (Figure 3 and figure S3), demonstrating that the BBCES measurements provide results

432   with both a wide wavelength range and high accuracy. Comparison of our measurements with *n*-

433   based calculations for these gases in the entire wavelength range of this study yields excellent

434   agreement with relative differences of 1.5% and 1.1%, 1.5%, 2.9%, and 1.4% on average,

435   respectively. The O_2-O_2 CIA cross-sections obtained from the BBCES measurements are

436   compared with those published by Thalman and Volkamer (2013). The relative differences are

437   within 1.1% at 477, 532, 577, 630 nm. Larger relative differences occur at the weak bands at 344

438   (4.2%), 360 (–29%), 380 (–21%), and 446 (4.2%) nm. The absorption cross-sections of CH_4 in the

439   wavelength range of 400-725 nm agree well with those documented by Giver (1978).

440   Rayleigh scattering cross-sections of CO_2 determined using BBCES in this study, and in other

441   studies have shown that the refractive index recommended by Sneep and Ubachs (2005) is suitable

442   for use in the wavelength range of 307–725 nm. By incorporating the refractive index data from

443   previous studies, we developed new dispersion relations for the refractive index of N_2O (307-725

444   nm), SF_6 (264–725 nm), and CH_4 (264–671 nm). The new dispersion relation for CH_4 captures the

445   measurements from BBCES more adequately.

446   Previous studies measured the Rayleigh scattering and absorption cross-sections of CO_2, N_2O,

447   O_2, SF_6, and CH_4 at narrow spectral ranges or single wavelengths. In this study, we used BBCES

448   that covers the broad wavelength range of 307–725 nm to measure total extinction (the sum of

449   absorption and scattering). The measurements validate that refractive index-based methods for

450   calculating Rayleigh extinction cross-sections are accurate and provide new fits over more

451   continuous and extended wavelengths range than available in the literature to constrain such

452   methods. The Rayleigh scattering cross-sections reported here are useful in several applications.

453   These include calibration standards based on extinction for optically-based instruments, such as

454   those designed for aerosol optical properties measurements or trace gas concentrations in the field

455   (Jordan et al., 2019; Min et al., 2016; Bluvshtein et al., 2017), especially when high-refractive

456   index gases are used for improved calibration. They will also improve the accuracy of Rayleigh

457   scattering parameterizations for major greenhouse gases in Earth's atmosphere, CO_2, CH_4, and

458   N_2O. Accurate quantitative measurements of Rayleigh scattering coefficients and absorption

459   cross-sections of atmospheric gases such as molecular N_2, O_2, CO_2 and the CIA of O_2–O_2 cross-

460   sections in the UV-NIR range are of particular importance for the application of Rayleigh LIDAR

461   systems, especially at the Nd:YAG laser harmonics 1064, 532 & 366 nm. These systems analyze

462   the molecular backscattering contributions to the LIDAR's attenuated backscatter signals to

463   retrieve the atmospheric profile of aerosols and clouds in the planetary boundary layer (Tomasi et

464   al., 2005; Herron, 2007). Recent NASA satellite missions have also aimed to measure global

465   carbon dioxide concentrations with high precision (0.25%) (Drouin et al., 2017). These CO_2 global

466   missions use the O_2–O_2 CIA underneath the structured O_2 A-band (760 nm) to evaluate the solar

467   radiation double pathlength in the Earth atmosphere and to determine the atmospheric pressure.

468   The measurements in this study validate the existing literature on the extinction of O_2 collision

469 complexes and molecular oxygen bands, and can be used for calibration purposes in both remote

470 sensing and *in-situ* spectroscopic applications in the atmosphere. In the future, gas extinction

471 measurements at extended wavelengths (near-infrared) and for additional gases (e.g., N_2) will

472 improve the spectroscopic applications in atmospheric studies.

473 **Data availability.**

474 Data are available upon request from the corresponding author (yinon.rudich@weizmann.ac.il).

475 **Author contributions.**

476 Q.H., S.S., and Y.R. designed this study. Q.H., Z.F., and O.S. conducted the experiments. Q.H.

477 prepared the draft and all of the co-authors reviewed it and provided comments.

478 **Competing interests.**

479 The authors declare that they have no conflict of interest.

480 **Acknowledgments**
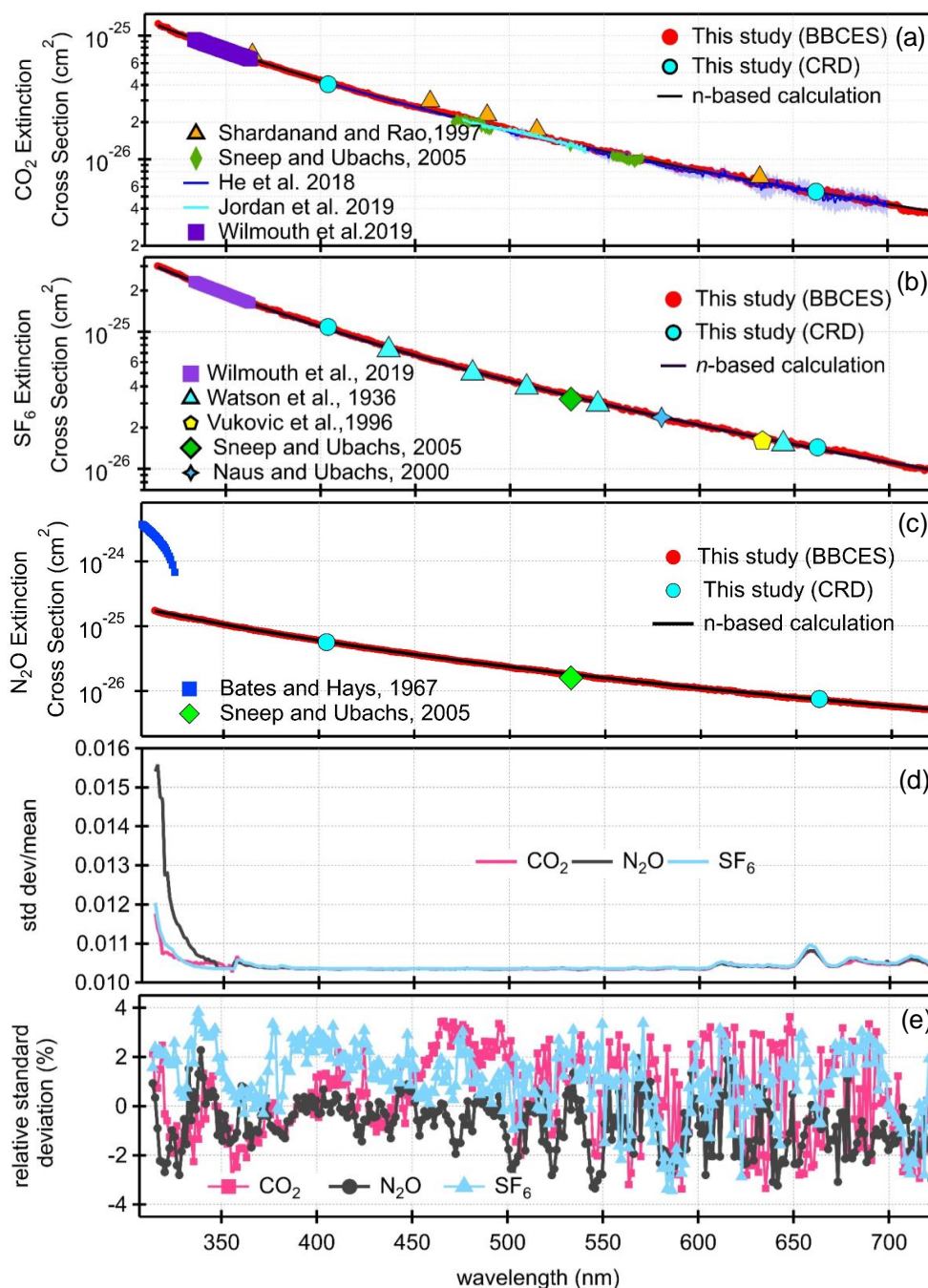
Figure 1. Rayleigh scattering cross-sections of CO_2 (a), SF_6 (b), and N_2O (c). Panel (d) shows the relative standard deviations as a function of wavelength for each gas. The relative difference in the cross-sections obtained by the BBCES and calculations from the refractive index are displayed (e).

Atmospheric
Chemistry
and Physics
Discussions
Open Access
EGU
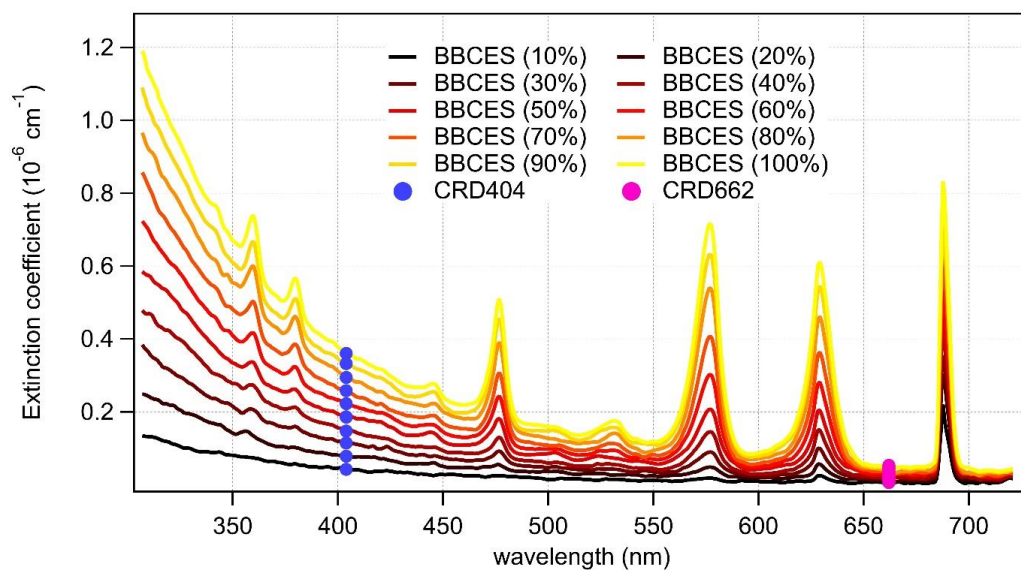
489

490 Figure 2. Wavelength-dependent extinction coefficients of O_2 + He mixtures as a function of O_2
491 concentration. The colored lines represent the extinction coefficients measured by BBCES, and
492 markers represent results from CRDS.
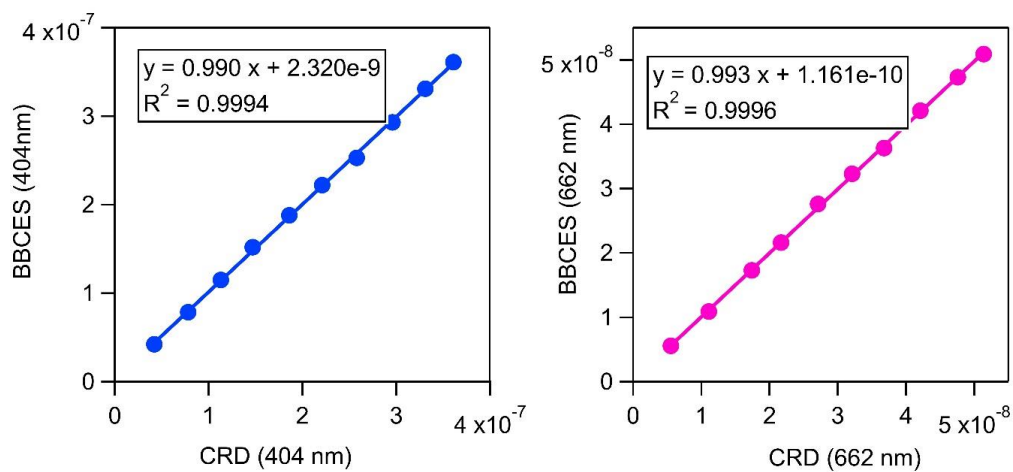
493

494 Figure 3. Correlations between the extinction coefficients (unit, cm^{-1}) measured by the BBCES
495 and CRDS.

Atmospheric
Chemistry
and Physics
Discussions

Open Access

EGU

wavelength	a	b	c
687.7 nm	-6.84e-48	2.86e-26	1.34 e-8
629.2 nm	7.29e-46	7.80e-27	-1.09e-10
577.2 nm	1.10e-45	5.27e-27	-1.41e-9
476.7 nm	6.66e-46	7.68e-27	1.53e-9

496
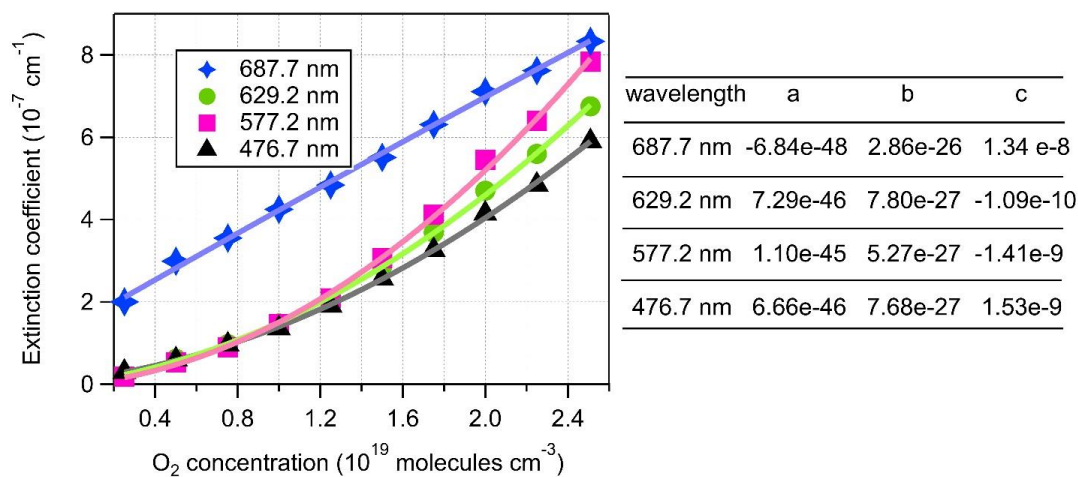
497 Figure 4. 2rd order polynomial fit of extinction coefficients measured by the BBCES. The O_2
498 concentration-dependent extinction coefficients are contributed by the extinction coefficients of
499 O_2 (σ_{O_2}), He (σ_{He}), and the O_2-O_2 CIA cross-sections ($\sigma_{O_2\text{-}O_2}$).

500
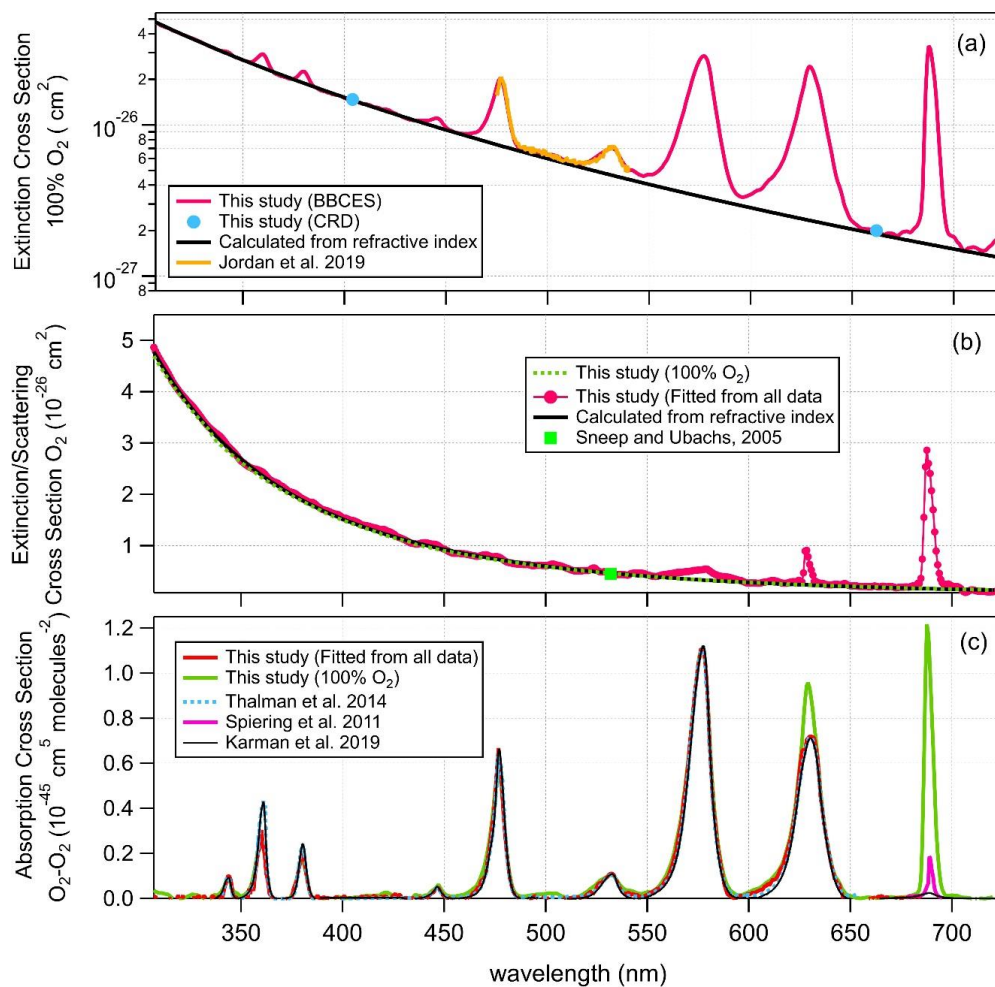
Figure 5. Wavelength-dependent extinction cross-sections of 100% O_2 (a), extinction cross-sections of O_2 (b), and O_2-O_2 CIA cross-section (c).

503
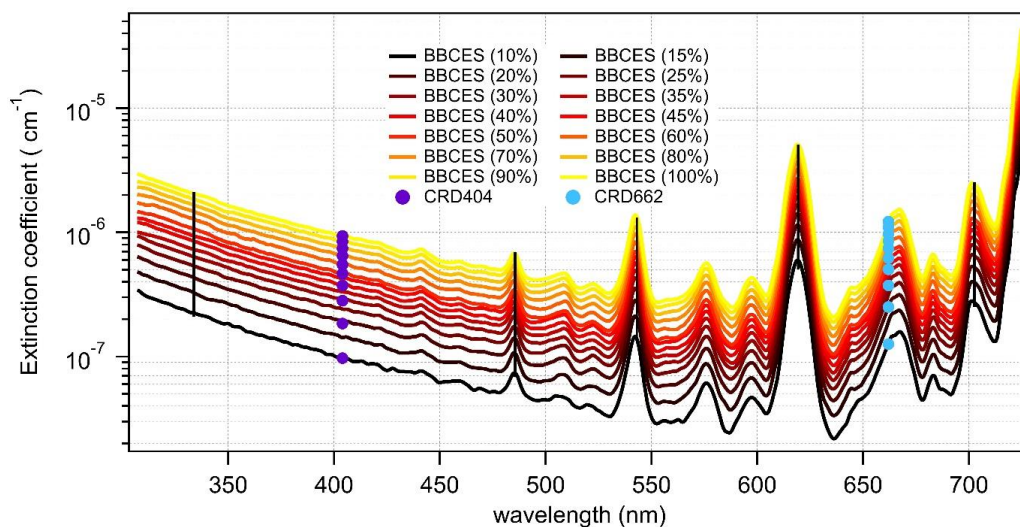
Figure 6. Wavelength-dependent extinction coefficients of CH_4 + He mixtures as a function of
CH_4 mixing ratio. The colored lines represent extinction coefficients obtained from BBCES and
markers represent results from CRDS. Measurements were performed with CH_4 percentage within
10% and 100% with a 10% step. Moreover, BBCES measurements were also performed for 15%,
25%, 35%, and 45% CH_4. The number concentration of 100% methane was 2.50143×10^{19}
molecules cm^{-3}. Data at selected wavelengths (vertical lines) are shown in Figure 7.

510
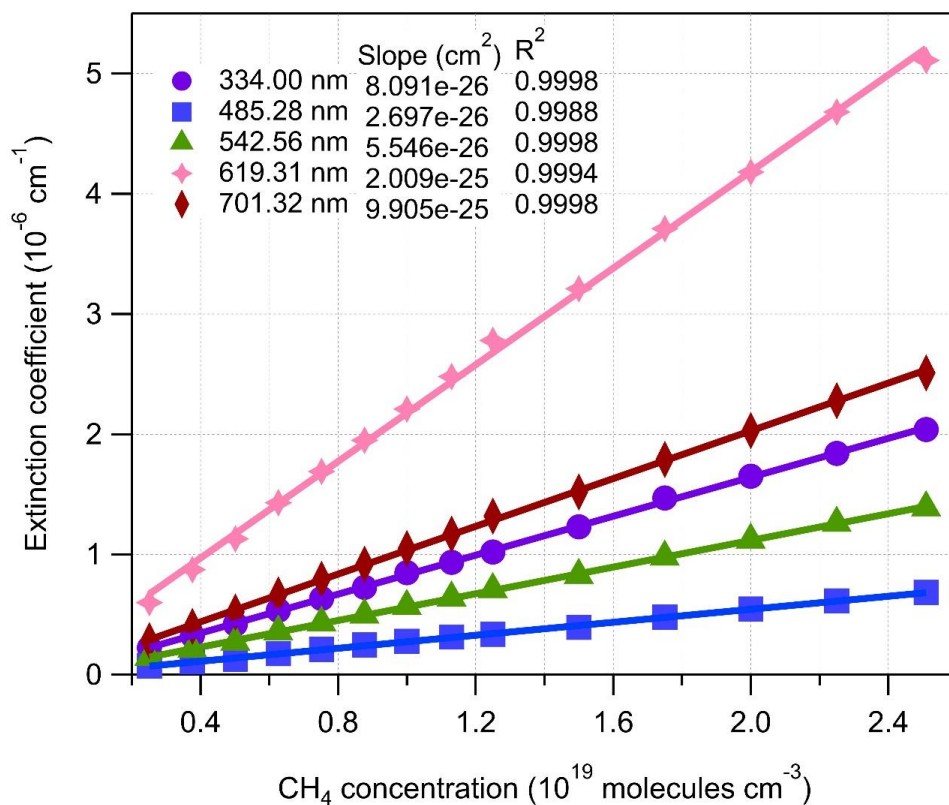
Figure 7. The relationship between BBCES measured extinction coefficients of CH_4+He mixtures
and CH_4 concentration. The selected wavelengths were located in Figure 6 by vertical lines.
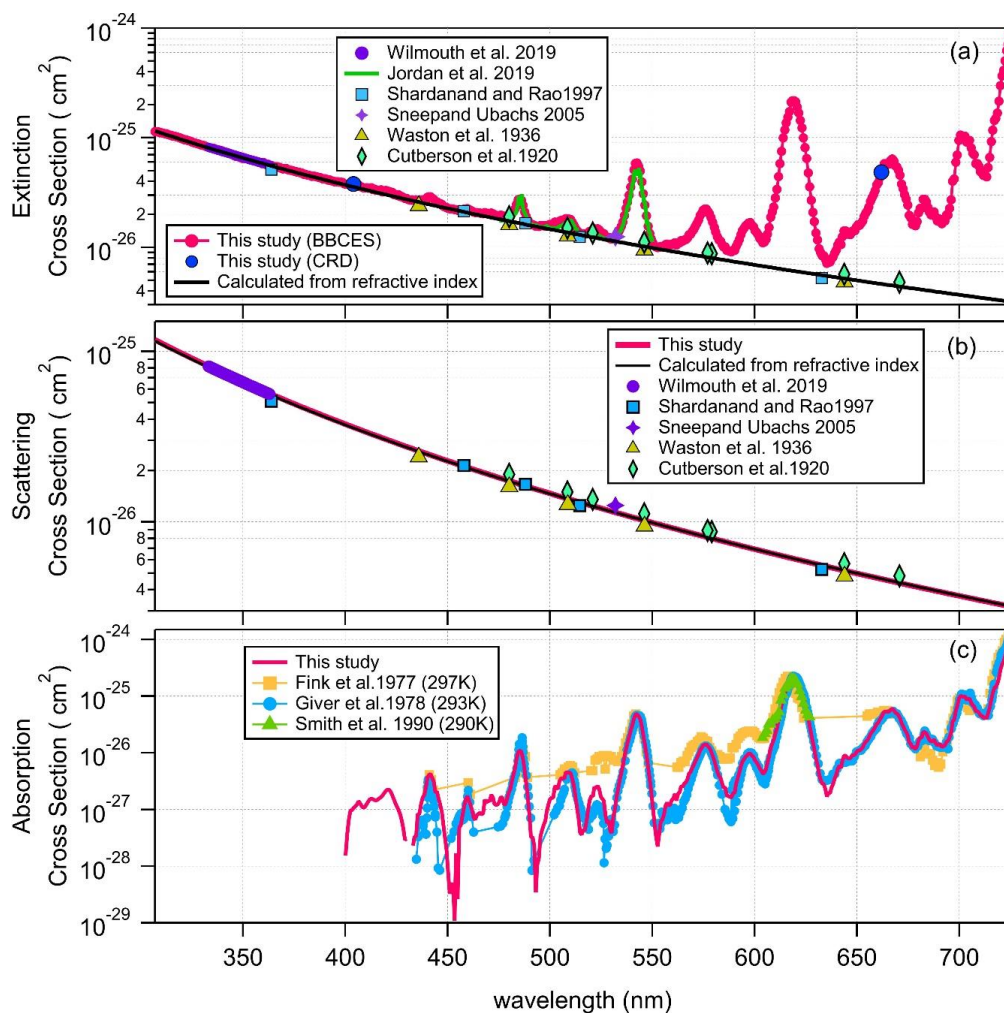
513

514   Figure 8. Extinction (a), scattering (b), and absorption (c) cross-sections of CH$_4$.

515
526
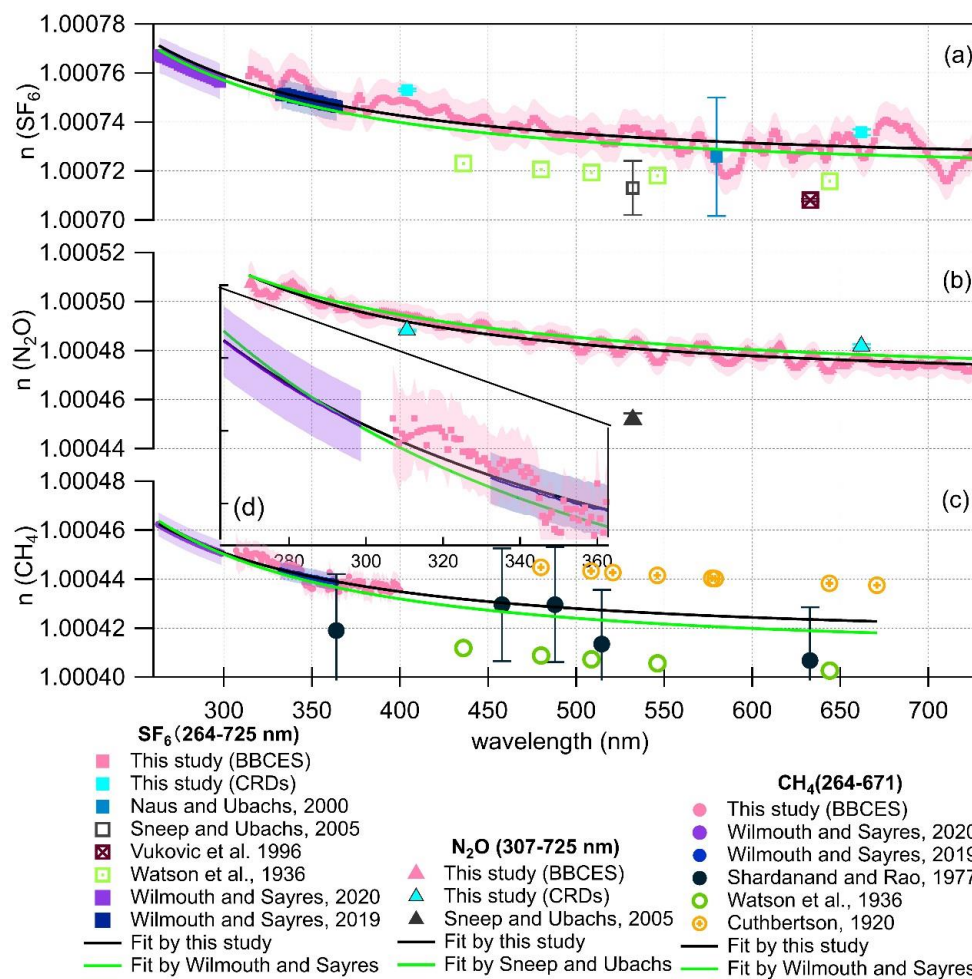
Figure
9. Real refractive index (n) for SF_6 (a), N_2O (b), and CH_4 (c). Comparison of Refractive index
from this work with previous studies (Cuthbertson and Cuthbertson, 1920; Naus and Ubachs, 2000;
Shardanand and Rao, 1977; Sneep and Ubachs, 2005; Vukovic et al., 1996; Watson et al., 1936;
Wilmouth and Sayres, 2019, 2020) over the wavelength range of 264–725 nm. The green line
represents the dispersion relation given in Table 1. The black line represents the dispersion relation
given in Eq. (8–10) derived from a fit to our data and references results. The n values for
Shardanand and Rao (1977), Sneep and Ubachs (2005), Naus and Ubachs (2000) were calculated
from their reported Rayleigh scattering cross-sections. Refractive index data from Sneep and
Ubachs (2005) are not used in the fitting since these results are away from others. Panel (d) is a
close-up view of the panel (c) in the wavelength range of 264–363 nm.

Atmospheric
Chemistry
and Physics
Discussions

527 Table 1. Refractive index and King correction factors for calculating Rayleigh scattering cross-
528 sections and available measurements in the wavelength range of 300–725 nm. Measurements for
529 He and N_2 are not summarized in this table.

Gas	Refractive index and King correction factors				Measurements	
	$(n-1) \times 10^8$	$F_k(\nu)$	ν (cm^{-1})	References	λ (nm)	References
He	$2283 + \dfrac{18102 \times 10^{13}}{1.5342 \times 10^{10} - \nu^2}$	1.0	14285-33333	Thalman, 2014; Leonard, 1974; Cuthbertson, 1932		
N_2	$5677.465 + \dfrac{318.81874 \times 10^{12}}{1.44 \times 10^{10} - \nu^2}$	$1.034 + 3.17 \times 10^{-12}\,\nu^2$	21360-39370	Sneep, 2005; Naus, 2000		
CO_2	$1.1427 \times 10^{11} \times \left(\dfrac{5799.25}{(128908.9)^2 - \nu^2} + \dfrac{120.05}{(89223.8)^2 - \nu^2} + \dfrac{5.3334}{(75037.5)^2 - \nu^2} + \dfrac{4.3244}{(67837.7)^2 - \nu^2} + \dfrac{1.218145 \times 10^{-5}}{(2418.136)^2 - \nu^2} \right)$	$1.1364 + 2.53 \times 10^{-11}\,\nu^2$	39417-55340	Alms, 1975; Bideau-Mehu, 1973; Sneep, 2005	333-725	Jordan, 2019; Shardanand, 1977; Sneep, 2005; Wilmouth, 2019; He, 2018
CH_4	$4869.8 + \dfrac{4.1023 \times 10^{14}}{1.133 \times 10^{10} - \nu^2}$	1.0	15385-40000	Sneep, 2005; Wilmouth, 2020	333-363, 434-725	Cuthbertson 1920; Jordan, 2019; Shardanand, 1977; Sneep, 2005; Watson, 1936; Wilmouth, 2019; Smith, 1990; Giver, 1978; Fink, 1977
N_2O	$46890 + 4.12 \times 10^{-6}\,\nu^2$	$\dfrac{3.3462 + 70.8 \times 10^{-12}\,\nu^2}{2.7692 - 47.2 \times 10^{-12}\,\nu^2}$	15453-21838	Alms, 1975; Sneep, 2005	300-320, 532	Johnston, 1975; Sneep, 2005
SF_6	$18611.4 + \dfrac{8.9566 \times 10^{14}}{1.680 \times 10^{10} - \nu^2}$	1.0	15385-40000	Sneep, 2005; Vukovic, 1996; Wilmouth, 2020	333-363, 532, 633	Sneep, 2005; Vukovic, 1996; Wilmouth, 2019
O_2 [a]	$20564.8 + \dfrac{2.480899 \times 10^{13}}{4.09 \times 10^9 - \nu^2}$	$1.09 + 1.385 \times 10^{-11}\,\nu^2 + 1.448 \times 10^{-20}\,\nu^4$	18315-34722	Hohm, 1993; Sneep, 2005	328-667	Thalman, 2013; Jordan, 2019; Hermans, 1999; Greenblatt, 1990; Spiering, 2011

530 Unless noted, the refractive index is scaled to 288.15 K and 1013.25 hPa. N = 2.546899 $\times 10^{19}$
531 molecules cm^{-3}.
532 Due to limited space, only the first name of each reference is shown in the table.
533 [a] The refractive index was obtained at 273.15 K and 1013.25 hPa, N = 2.68678 $\times 10^{19}$ molecules
534 cm^{-3} is used in Eq. (1)

Table 2. The Rayleigh scattering cross-sections (10^{-27} cm^2) calculated from the refractive index (*n*-based) and obtained from BBCES (Exp) of selected wavelengths.

λ(nm)	CO_2		SF_6		N_2O		O_2		CH_4	
	n-based	Exp	*n*-based	Exp	*n*-based	Exp	*n*-based	Exp	*n*-based	Exp
330	98.22	96.8	241.5	239.4	137.9	136.7	34.71	35.1	84.12	85.3
404	41.67	41.6	104.5	105.7	57.71	57.9	14.57	14.8	35.57	35.9
532	13.32	13.3	33.92	34.1	18.19	18.3	4.642	4.55	11.34	11.3
660	5.516	5.52	14.16	14.2	7.483	7.47	1.924	1.95	4.693	4.68
710	4.101	4.08	10.55	10.4	5.551	5.48	1.430	1.41	3.487	3.47

References

Alms, G. R., Burnham, A. K., and Flygare, W. H.: Measurement of the dispersion in polarizability anisotropies, J. Chem. Phys., 63, 3321-3326, 10.1063/1.431821, 1975.

Baidar, S., Oetjen, H., Coburn, S., Dix, B., Ortega, I., Sinreich, R., and Volkamer, R.: The CU Airborne MAX-DOAS instrument: vertical profiling of aerosol extinction and trace gases, Atmos. Meas. Tech., 6, 719-739, 10.5194/amt-6-719-2013, 2013.

Bates, D. R., and Hays, P. B.: Atmospheric nitrous oxide, Plan. Space Sci., 15, 189-197, 10.1016/0032-0633(67)90074-8, 1967.

Bideau-Mehu, A., Guern, Y., Abjean, R., and Johannin-Gilles, A.: Interferometric determination of the refractive index of carbon dioxide in the ultraviolet region, Opt. Commun., 9, 432-434, 10.1016/0030-4018(73)90289-7, 1973.

Bluvshtein, N., Flores, J. M., Segev, L., and Rudich, Y.: A new approach for retrieving the UV–vis optical properties of ambient aerosols, Atmos. Meas. Tech., 9, 3477-3490, 10.5194/amt-9-3477-2016, 2016.

Bluvshtein, N., Lin, P., Flores, J. M., Segev, L., Mazar, Y., Tas, E., Snider, G., Weagle, C., Brown, S. S., Laskin, A., and Rudich, Y.: Broadband optical properties of biomass-burning aerosol and identification of brown carbon chromophores, J. Geophys. Res. Atmos., 122, 5441-5456, 10.1002/2016JD026230, 2017.

Cuthbertson, C., and Cuthbertson, M.: On the refraction and dispersion of carbon dioxide, carbon monoxide, and methane, Proc. R. Soc. Lond. A, 97, 152-159, 10.1098/rspa.1920.0020, 1920.

Cuthbertson, C., and Cuthbertson, M.: The refraction and dispersion of neon and helium, Proc. R. Soc. Lond. A, 135, 40-47, 10.1098/rspa.1932.0019, 1932.

Drouin, B. J., Benner, D. C., Brown, L. R., Cich, M. J., Crawford, T. J., Devi, V. M., Guillaume, A., Hodges, J. T., Mlawer, E. J., Robichaud, D. J., Oyafuso, F., Payne, V. H., Sung, K., Wishnow, E. H., and Yu, S.: Multispectrum analysis of the oxygen A-band, J. Quant. Spectrosc. Radiat. Transf., 186, 118-138, 10.1016/j.jqsrt.2016.03.037, 2017.

Fink, U., Benner, D. C., and Dick, K. A.: Band model analysis of laboratory methane absorption spectra from 4500 to 10500 Å, J. Quant. Spectrosc. Radiat. Transf., 18, 447-457, 10.1016/0022-4073(77)90077-2, 1977.

Fuchs, H., Dube, W. P., Lerner, B. M., Wagner, N. L., Williams, E. J., and Brown, S. S.: A Sensitive and Versatile Detector for Atmospheric NO_2 and NOx Based on Blue Diode Laser Cavity Ring-Down Spectroscopy, Environ. Sci. Technol., 43, 7831-7836, 10.1021/es902067h, 2009.

Giver, L. P.: Intensity measurements of the CH4 bands in the region 4350 Å to 10,600 Å, J. Quant. Spectrosc. Radiat. Transf., 19, 311-322, 10.1016/0022-4073(78)90064-X, 1978.

Gordon, I. E., Rothman, L. S., Hill, C., Kochanov, R. V., Tan, Y., Bernath, P. F., Birk, M., Boudon, V., Campargue, A., Chance, K. V., Drouin, B. J., Flaud, J. M., Gamache, R. R., Hodges, J. T., Jacquemart, D., Perevalov, V. I., Perrin, A., Shine, K. P., Smith, M. A. H., Tennyson, J., Toon, G. C., Tran, H., Tyuterev, V. G., Barbe, A., Császár, A. G., Devi, V. M., Furtenbacher, T., Harrison, J. J., Hartmann, J. M., Jolly, A., Johnson, T. J., Karman, T., Kleiner, I., Kyuberis, A. A., Loos, J., Lyulin, O. M., Massie, S. T., Mikhailenko, S. N., Moazzen-Ahmadi, N., Müller, H. S. P., Naumenko, O. V., Nikitin, A. V., Polyansky, O. L., Rey, M., Rotger, M., Sharpe, S. W., Sung, K., Starikova, E., Tashkun, S. A., Auwera, J. V., Wagner, G., Wilzewski, J., Wcisło, P., Yu, S., and Zak, E. J.: The HITRAN2016 molecular spectroscopic database, J. Quant. Spectrosc. Radiat. Transf., 203, 3-69, https://doi.org/10.1016/j.jqsrt.2017.06.038, 2017.

Atmospheric
Chemistry
and Physics
Discussions

Greenblatt, G. D., Orlando, J. J., Burkholder, J. B., and Ravishankara, A. R.: Absorption measurements of oxygen between 330 and 1140 nm, J. Geophys. Res. Atmos., 95, 18577-18582, 10.1029/JD095iD11p18577, 1990.

He, Q., Bluvshtein, N., Segev, L., Meidan, D., Flores, J. M., Brown, S. S., Brune, W., and Rudich, Y.: Evolution of the Complex Refractive Index of Secondary Organic Aerosols during Atmospheric Aging, Environ. Sci. Technol., 52, 3456-3465, 10.1021/acs.est.7b05742, 2018.

Hermans, C., Vandaele, A. C., Carleer, M., Fally, S., Colin, R., Jenouvrier, A., Coquart, B., and Mérienne, M.-F.: Absorption cross-sections of atmospheric constituents: NO2, O2, and H2O, Environ. Sci. Pollut. Res., 6, 151-158, 10.1007/BF02987620, 1999.

Herron, J. P.: Rayleigh-Scatter Lidar Observations at USU's Atmospheric Lidar Observatory (Logan,UT) - Temperature Climatology, Temperature Comparisons with MSIS, and Noctilucent Clouds, Doctor of Philosophy (PhD), Utah State University, 2007.

Hohm, U.: Experimental determination of the dispersion in the mean linear dipole polarizability $\alpha(\omega)$ of small hydrocarbons and evaluation of Cauchy moments between 325 nm and 633 nm, Mol. Phys., 78, 929-941, 10.1080/00268979300100621, 1993.

Ityaksov, D., Linnartz, H., and Ubachs, W.: Deep-UV Rayleigh scattering of N_2, CH_4 and SF_6, Mol. Phys., 106, 2471-2479, 10.1080/00268970802570334, 2008a.

Ityaksov, D., Linnartz, H., and Ubachs, W.: Deep-UV absorption and Rayleigh scattering of carbon dioxide, Chem. Phys. Lett., 462, 31-34, 10.1016/j.cplett.2008.07.049, 2008b.

Johnston, H. S., and Selwyn, G. S.: New cross sections for the absorption of near ultraviolet radiation by nitrous oxide (N_2O), Geophys. Res. Lett., 2, 549-551, 10.1029/GL002i012p00549, 1975.

Jordan, N., Ye, C. Z., Ghosh, S., Washenfelder, R. A., Brown, S. S., and Osthoff, H. D.: A broadband cavity-enhanced spectrometer for atmospheric trace gas measurements and Rayleigh scattering cross sections in the cyan region (470–540 nm), Atmos. Meas. Tech., 12, 1277-1293, 10.5194/amt-12-1277-2019, 2019.

King, L. V., and Eve, A. S.: On the complex anisotropic molecule in relation to the dispersion and scattering of light, Proc. R. Soc. Lond. A, 104, 333-357, 10.1098/rspa.1923.0113, 1923.

Leonard, P. J.: Refractive indices, Verdet constants, and Polarizabilities of the inert gases, At. Data Nucl. Data Tables, 14, 21-37, 10.1016/s0092-640x(74)80028-8, 1974.

Long, C. A., and Ewing, G. E.: Spectroscopic investigation of van der Waals molecules. I. The infrared and visible spectra of $(O_2)_2$, J. Chem. Phys., 58, 4824-4834, 10.1063/1.1679066, 1973.

Min, K. E., Washenfelder, R. A., Dube, W. P., Langford, A. O., Edwards, P. M., Zarzana, K. J., Stutz, J., Lu, K., Rohrer, F., Zhang, Y., and Brown, S. S.: A broadband cavity enhanced absorption spectrometer for aircraft measurements of glyoxal, methylglyoxal, nitrous acid, nitrogen dioxide, and water vapor, Atmos. Meas. Tech., 9, 423-440, 10.5194/amt-9-423-2016, 2016.

Naus, H., and Ubachs, W.: Experimental verification of Rayleigh scattering cross sections, Opt. Lett., 25, 347-349, 10.1364/OL.25.000347, 2000.

Newnham, D. A., and Ballard, J.: Visible absorption cross sections and integrated absorption intensities of molecular oxygen (O2 and O4), J. Geophys. Res. Atmos., 103, 28801-28815, 10.1029/98JD02799, 1998.

Platt, U., and Stutz, J.: Differential Optical Absorption Spectroscopy, in: Physics of Earth and Space Environments, Springer Berlin Heidelberg, 2008.

Shardanand, S., and Rao, A. D. P.: Absolute Rayleigh scattering cross sections of gases and freons of stratospheric interest in the visible and ultraviolet regions, NASA Technical Note, 1977.

Smith, W. H., Conner, C. P., and Baines, K. H.: Absorption-Coefficients for the 6190-a Ch4-Band between 290-Degrees-K and 100-Degrees-K with Application to Uranus Atmosphere, Icarus, 85, 58-64, 10.1016/0019-1035(90)90103-G, 1990.

Sneep, M., and Ubachs, W.: Direct measurement of the Rayleigh scattering cross section in various gases, J. Quant. Spectrosc. Ra., 92, 293-310, 10.1016/j.jqsrt.2004.07.025, 2005.

Spiering, F. R., Kiseleva, M. B., Filippov, N. N., van Kesteren, L., and van der Zande, W. J.: Collision-induced absorption in the O2 B-band region near 670 nm, Phys. Chem. Chem. Phys., 13, 9616-9621, 10.1039/C1CP20403C, 2011.

Strutt, J. W.: XXXIV. On the transmission of light through an atmosphere containing small particles in suspension, and on the origin of the blue of the sky, London, Edinburgh Dublin Philos. Mag. J. Sci., 47, 375-384, 10.1080/14786449908621276, 1899.

Strutt, R. J.: The light scattered by gases: its polarisation and intensity, Proc. R. Soc. Lond. A, 95, 155-176, 10.1098/rspa.1918.0057, 1918.

Strutt, R. J.: A re-examination of the light scattered by gases in respect of polarisation. I.- Experiments on the common gases, Proc. R. Soc. Lond. A, 97, 435-450, 10.1098/rspa.1920.0044, 1920.

Thalman, R., and Volkamer, R.: Temperature dependent absorption cross-sections of O_2–O_2 collision pairs between 340 and 630 nm and at atmospherically relevant pressure, Phys. Chem. Chem. Phys., 15, 15371-15381, 10.1039/C3CP50968K, 2013.

Thalman, R., Zarzana, K. J., Tolbert, M. A., and Volkamer, R.: Rayleigh scattering cross-section measurements of nitrogen, argon, oxygen and air, J. Quant. Spectrosc. Ra., 147, 171-177, 10.1016/j.jqsrt.2014.05.030, 2014.

Tomasi, C., Vitale, V., Petkov, B., Lupi, A., and Cacciari, A.: Improved algorithm for calculations of Rayleigh-scattering optical depth in standard atmospheres, Appl. Opt., 44, 3320-3341, 10.1364/AO.44.003320, 2005.

Vukovic, D., Woolsey, G. A., and Scelsi, G. B.: Refractivities of and at wavelengths of 632.99 and 1300 nm, Journal of Physics D: Applied Physics, 29, 634-637, 10.1088/0022-3727/29/3/023, 1996.

Washenfelder, R. A., Langford, A. O., Fuchs, H., and Brown, S. S.: Measurement of glyoxal using an incoherent broadband cavity enhanced absorption spectrometer, Atmos. Chem. Phys., 8, 7779-7793, 10.5194/acp-8-7779-2008, 2008.

Washenfelder, R. A., Flores, J. M., Brock, C. A., Brown, S. S., and Rudich, Y.: Broadband measurements of aerosol extinction in the ultraviolet spectral region, Atmos. Meas. Tech., 6, 861-877, 10.5194/amt-6-861-2013, 2013.

Washenfelder, R. A., Attwood, A. R., Flores, J. M., Zarzana, K. J., Rudich, Y., and Brown, S. S.: Broadband cavity-enhanced absorption spectroscopy in the ultraviolet spectral region for measurements of nitrogen dioxide and formaldehyde, Atmos. Meas. Tech., 9, 41-52, 10.5194/amt-9-41-2016, 2016.

Watson, H. E., Ramaswamy, K. L., and Donnan, F. G.: The refractive index dispersion and polarization of gases, Proceedings of the Royal Society of London. Series A - Mathematical and Physical Sciences, 156, 144-157, 10.1098/rspa.1936.0140, 1936.

Wilmouth, D. M., and Sayres, D. S.: Rayleigh scattering cross sections of argon, carbon dioxide, sulfur hexafluoride, and methane in the UV-A region using Broadband Cavity Enhanced Spectroscopy, J. Quant. Spectrosc. Radiat. Transf., 234, 32-39, 10.1016/j.jqsrt.2019.05.031, 2019.

Wilmouth, D. M., and Sayres, D. S.: Determination of Rayleigh scattering cross sections and indices of refraction for Ar, CO_2, SF_6, and CH_4 using BBCES in the ultraviolet, J. Quant. Spectrosc. Radiat. Transf., 107224, 10.1016/j.jqsrt.2020.107224, 2020.